RSC Advances

PAPER

View Article Online
View Journal | View Issue

Cite this: *RSC Adv.*, 2022, **12**, 35809

T_1–T_2 dual-modal magnetic resonance contrast-enhanced imaging for rat liver fibrosis stage†

Fulin Lu,[ab] Liang Du,[a] Wei Chen,[a] Hai Jiang,[a] Chenwu Yang,[a] Yu Pu,[a] Jun Wu,[a] Jiang Zhu,[a] Tianwu Chen,[a] Xiaoming Zhang*[a] and Changqiang Wu *[a]

The development of an effective method for staging liver fibrosis has always been a hot topic of research in the field of liver fibrosis. In this paper, PEGylated ultrafine superparamagnetic iron oxide nanocrystals (SPIO@PEG) were developed for T_1–T_2 dual-modal contrast-enhanced magnetic resonance imaging (MRI) and combined with Matrix Laboratory (MATLAB)-based image fusion for staging liver fibrosis in the rat model. Firstly, SPIO@PEG was synthesized and characterized with physical and biological properties as a T_1–T_2 dual-mode MRI contrast agent. Secondly, in the subsequent MR imaging of liver fibrosis in rats *in vivo*, conventional T_1 and T_2-weighted imaging, and T_1 and T_2 mapping of the liver pre- and post-intravenous administration of SPIO@PEG were systematically collected and analyzed. Thirdly, by creative design, we fused the T_1 and T_2 mapping images by MATLAB and quantitively measured each rat's hepatic fibrosis positive pixel ratio (PPR). SPIO@PEG was proved to have an ultrafine core size (4.01 ± 0.16 nm), satisfactory biosafety and T_1–T_2 dual-mode contrast effects under a 3.0 T MR scanner (r_2/r_1 = 3.51). According to the image fusion results, the SPIO@PEG contrast-enhanced PPR shows significant differences among different stages of liver fibrosis (P < 0.05). The combination of T_1–T_2 dual-modal SPIO@PEG and MATLAB-based image fusion technology could be a promising method for diagnosing and staging liver fibrosis in the rat model. PPR could also be used as a non-invasive biomarker to diagnose and discriminate the stages of liver fibrosis.

Received 19th September 2022
Accepted 2nd December 2022

DOI: 10.1039/d2ra05913d

rsc.li/rsc-advances

1 Introduction

Cholestatic liver fibrosis has quickly become a research hotspot with an increased relationship to the mechanism of liver cirrhosis and liver failure associated with severe morbidity and mortality.[1–4] However, despite treatment, some biliary liver fibrotic patients progress toward liver cirrhosis or other end-stage liver diseases.[5] At present, the gold standard method for detecting and staging liver fibrosis in clinical practice is liver biopsy, which is limited by obvious bias, sampling error, and high cost.[6] Moreover, a biopsy is an invasive method with infection risk and other significant complications that are not suitable for dynamic observation and repeating examinations.[7] Traditional diffusion-weighted imaging (DWI) and ultrasound transient elastography are two diagnostic techniques for liver fibrosis with the greatest potential.[8] Nevertheless, both methods have inherent drawbacks: the diffusion of water molecules affects DWI, and ultrasound transient elastography has poor imaging quality. Notably, both methods are single-mode imaging techniques and their diagnosis and staging abilities could be significantly limited.[9,10] For these reasons, noninvasive multi-mode imaging techniques that can repeatedly evaluate liver fibrosis throughout the entire organ hold great promise for a more accurate assessment of the fibrosis burden and progression, and treatment response is desperately needed on a clinical basis.

Great efforts have been made to develop a non-invasive and highly effective method for diagnosing and staging liver fibrosis.[11–13] However, single-mode image modality provides limited information and cannot meet the requirements of complex disease diagnoses, surgery, and radiation therapy.[14] Among the existing techniques, magnetic resonance imaging (MRI) is considered a powerful multi-mode imaging technology, which includes T_1 mapping, T_2 mapping, magnetic resonance spectroscopy, *etc.*, and can be used to evaluate the patient from different aspects and make cross-validation for diseases.[15,16] For example, the T_1–T_2 dual-mode contrast-enhanced imaging can provide both T_1 and T_2 information to effortlessly distinguish the focal lesions from the normal tissue with fault-free and self-confirming MR images. The combination of T_1 and T_2 imaging modes might be a potential strategy since this method can double-check the obtained imaging data, yielding

[a]*Medical Imaging Key Laboratory of Sichuan Province, School of Medical Imaging, Affiliated Hospital of North Sichuan Medical College, Nanchong 637000, China. E-mail: wucq1984@nsmc.edu.cn*

[b]*Department of Radiology, Sichuan Academy of Medical Sciences, Sichuan Provincial People's Hospital, University of Electronic Science and Technology of China, Chengdu 610072, China*

† Electronic supplementary information (ESI) available. See DOI: https://doi.org/10.1039/d2ra05913d

complementary information for sensitive and accurate MRI.[17] Furthermore, the measurement of T_1 and T_2 relaxation times by using T_1 and T_2 mapping may be more objective and reliable for qualifying the quantitative evaluation of the relaxation time of liver parenchyma in the progression of liver fibrosis.[18,19]

Superparamagnetic iron oxide (SPIO) with good biosafety and low toxicity is commonly studied as a T_2 contrast agent for the liver. However, the negative contrast effect and low signal-to-noise ratio make the widespread application in clinical settings difficult.[20] Previous studies have demonstrated that the crystal size, surface coating, and aggregation state of SPIO are significantly related to its relaxivities (r_2 and r_1) and r_2/r_1 ratio, and SPIO nanoparticles with appropriate sizes and magnetizations could inherently display both T_1 and T_2 contrasts.[21–23] They found that the ultrafine size of SPIO nanoparticles would lead to T_1-dominated contrast efficiency. The T_1 effect of SPIO is likely attributed to (i) the reduced magnetization, which diminishes the T_2 decaying effect, and (ii) the enhanced surface-to-volume ratio, which provides a large number of paramagnetic centers on the surface.[24,25] Moreover, our previous study found that monodisperse ultrafine PEGylated SPIO nanocrystals (SPIO@PEG) have a high T_1 relaxivity and a modest r_2/r_1 ratio (<10) at the magnetic field of 3.0 T and could be potentially used as a T_1–T_2 dual-modal MRI contrast agent.[26] Ultrafine MR nano-contrast agents that combine the advantages of both T_1 and T_2 imaging modalities could be the key to the highly accurate and sensitive diagnosis and staging of liver fibrosis.

Herein, we have investigated the diagnosis and stage performance of SPIO@PEG nanoparticles as a T_1–T_2 dual-modal MR contrast agent for liver fibrosis under a clinical 3.0 T MR scanner. Based on the T_1 and T_2 mapping technology, we first fused the T_1 mapping and T_2 mapping images to verify the power of the double-checking process in the field of liver fibrosis in the rat model.

2 Materials and methods

2.1 Synthesis of PEGylated ultrafine superparamagnetic iron oxide nanocrystals

Ultrafine SPIO@PEG was prepared as previously reported.[26,27] In brief, hydrophobic SPIO nanocrystals were synthesized by the high-temperature thermal decomposition of iron acetylacetonate, and the small crystal size was obtained by controlling the reaction heating conditions. After that, SPIO nanocrystals were transferred to the aqueous phase by a ligand exchange reaction with sodium citrate. Subsequently, polyethylene glycol dopamine (PEG-DA) was coated on the surface of SPIO nanocrystals in an aqueous environment (for synthesis details, see ESI†). The crystal size and dispersity were examined using transmission electron microscopy (TEM, Thermo Fisher Scientific, USA), selected area electron diffraction (SAED, Thermo Fisher Scientific, USA) and dynamic light scattering (DLS, Malvern Panalytical, UK). Fourier transform infrared spectroscopy (FTIR, Thermo Nicolet, USA) was used to test for the characteristic absorption peak of PEG in SPIO@PEG nanoparticles. The composition of SPIO@PEG was determined by atomic absorption spectroscopy (AAS).

2.2 *In vitro* MRI study of ultrafine SPIO@PEG nanoparticles

Ultrafine SPIO@PEG aqueous samples with different Fe concentrations (0.05, 0.1, 0.2, 0.3, 0.4, and 0.5 mmol L^{-1}) were prepared and placed in 2 mL test bottles. Longitudinal and transverse relaxation times (T_1 and T_2) were measured at room temperature at 0.5 T (magnetic resonance developer relaxation rate analyzer, NIUMAG, Suzhou, China), 1.5 T (Minispec Mq60 NMR Analyzer, Bruker, Beijing, China), and 3.0 T (Discovery MR750, GE Medical System, Milwaukee, WI), respectively. The T_1 and T_2 relaxivities (r_1 and r_2, mM^{-1} s^{-1}) were determined by the curve fitting of T_1 and T_2 *vs.* Fe concentration. MR imaging of samples was performed under a clinical 3.0 T MR scanner (Discovery MR750, GE Medical System, Milwaukee, WI). Axial images of the phantoms were acquired by T_1-weighted spin-echo sequence (repetition time = 200 ms, echo time = 9 ms, matrix = 320 × 320, field of view = 18 × 18 cm, slice thickness = 3 mm, flip angle = 90°) and T_2-weighted spin echo sequence (repetition time = 2500 ms, echo time = 100 ms, matrix = 320 × 320, field of view = 18 × 18 cm, slice thickness = 3 mm, flip angle = 90°).

2.3 Cytotoxicity assay

Cytotoxicity on the mouse macrophage cell line Raw 264.7 and serum stability of SPIO@PEG were determined in our previous study.[20] We further tested the cytotoxicity of SPIO@PEG nanoparticles on hepatic cancer cells (Hep G2). Hep G2 was provided by the Chinese Academy of Sciences Cell Bank (Shanghai, China). The cells were cultured in Dulbecco's Modified Eagle's Medium (DMEM)/high glucose (4.5 g L^{-1} glucose) containing 10% (v/v) fetal bovine serum (Biological Industries, Israel) and 1% (v/v) penicillin–streptomycin (Hyclone, Logan, UT) at 37 °C, 5% CO_2, and saturated humidity. Hep G2 cells were plated in 96-well plates at 4 × 10^3 cells per well (100 μL) of complete medium and incubated for 24 h. The cells were added with varying Fe concentrations (5, 10, 15, and 20 μg mL^{-1}) of SPIO@PEG nanoparticles and with subsequent incubation for 24 h. Afterward, to each well was added a 10 μL Cell Counting Kit-8 (CCK-8) solution (Boster Biological Technology, Wuhan, China), followed by incubation at 37 °C for 1 h. The absorbance of the samples was measured using a microplate reader (Thermo Scientific, USA). Cell viability was calculated according to the following equation:

$$\text{Cell viability (\%)} = (N_S/N_C) \times 100\% \quad (1)$$

where N_S and N_C are the absorbances of living cells treated with or without SPIO@PEG nanoparticles. The absorbance measurements were used and corrected as the blank control group.

2.4 Animal liver fibrosis model

This study has been approved by the Animal Ethics Committee of North Sichuan Medical College (NSMC-2021-79). All experimental procedures were followed in strict accordance with the proposal in the Guide for the Care and Use of Laboratory Animals of the National Institutes of Health. Healthy male

Sprague-Dawley (SD) rats (180–200 g and 6–7 weeks old) were obtained from the Experimental Animal Center of our institute. Twenty-eight rats were randomly divided into the control group and four experimental groups. The control group rats ($n = 7$) were fed a standard commercial diet. The four experimental groups were fed a 0.1% 3,5-diethoxycarbonyl-1,4-dihydrocollidine (DDC) supplemented diet (Tokyo Chemical Industry, Co., Ltd, Tokyo, Japan) for 1 week, 4 weeks, 8 weeks and 12 weeks, respectively, to build different stages of the biliary liver fibrotic model.[28] All animals were raised at 23 ± 3 °C with a 12 h:12 h light/dark cycle and tap water ad libitum.

2.5 *In vivo* MR imaging

All MR imaging was performed using a 3.0 T MRI scanner (GE Healthcare, MR750 Medical System, Milwaukee, WI). The rats were anesthetized *via* the inhalation of isoflurane (RWD Life Science, Shenzhen, China) with a face mask (anesthetic conc.: 1.0–1.5%; 20–30 mL O_2 per kg) and transferred to the MR scanner. A custom-made animal receiver coil was used to obtain the MR images. MRI scans were carried out before (pre) and immediately after (post) SPIO@PEG intravenous injection at a dose of 2.5 mg (Fe concentration) kg^{-1} body weight through the tail veins of the rats. Conventional T_1 and T_2 weighted MR imaging was also performed pre- and post-contrast injection, and the detailed parameters of T_1 and T_2-weighted sequences were as follows: T_1 weighted imaging (gradient recalled echo sequence, repetition time (T_R) = 9 ms, echo time (T_E) = 3 ms, flip angle (FA) = 30°, field of view (FOV) = 80 × 80 mm); T_2 weighted imaging (fast spin echo sequence, T_R = 4000 ms, T_E = 76 ms, FA = 90°, FOV = 80 × 80 mm and slice thickness = 2.0 mm).

T_1 mapping images were acquired by using the variable flip angle (VFA) technique[29] that contains a series of rat liver acquisition volume accelerations (LAVA) with five different flip angles (3, 6, 9, 12, and 15°). The following are the MR imaging parameters: T_R = 5.0 ms, T_E = 2.4 ms, number of excitations = 4, FOV = 80 × 80 mm, matrix = 512 × 512, reconstruction matrix = 400 × 400, bandwidth = 83.33 Hz per pixel, slice thickness = 0.8 mm. T_2 mapping images were acquired by using free-breathing fast spin echo (FES) sequences; the detailed parameters were as follows: T_R = 1200 ms, T_E = 8, 16, 24, 32, 40, 48, 56, and 64 ms, number of excitations = 2, FA = 90°, FOV = 80 × 80 mm, matrix = 512 × 512, reconstruction matrix = 400 × 400, bandwidth = 166.67 Hz per pixel, thickness = 2.0 mm, slice space = 0.6 mm.

2.6 Image analysis

Two radiologists with diagnosis experience of three and fourteen, respectively, performed image analyses; they were blinded to both the animal groups and pathological results of this study. The conventional T_1 and T_2 weighted MR images, including the pre- and post-contrast images, were presented on a picture archiving and communication system (PACS; GE Advantage Workstation Version 4.4-09, Sun Microsystems, Palo Alto, CA, USA) with an optimal window setting adjustment. Subsequently, we measured each experimental rat's signal-to-noise ratio (SNR = mean signal intensity of the liver/background noise). Furthermore, based on the SNR measurements, the contrast-to-noise ratio ($\Delta CNR = abs(SNR_{pre} - SNR_{post})$) as described by Siedek F. *et al.*[30] was calculated for each rat, including T_1 and T_2 weighted MR images pre- and post-SPIO@PEG enhancement (ΔCNR-T_1 and ΔCNR-T_2, respectively).

T_1 mapping and T_2 mapping images, including pre- and post-contrast images, were transferred to the matrix laboratory (MATLAB, version 9.7 (R2019b), Mathworks, USA) for the next analysis. T_1 relaxation times were measured by the VFA method, which has been demonstrated by Deoni S. C. *et al.*[29] (Fig. S2, see ESI†). T_2 relaxation times were calculated by a monoexponential function model, which was used to fit the T_2 signal *versus* echo time (TE) decay curve[31] (Fig. S3, see ESI†). Three regions of interest (ROIs) of one section were respectively drawn within the liver parenchyma and constantly measured on five liver sections of each rat, avoiding confounding factors like biliary structures, vessels, and organ boundaries. The size of ROI was controlled within 0.8–1.2 cm^2. The ROIs were first placed into the pre-contrast T_1 and T_2 mapping, then the ROIs were copied and placed on the same area on post-contrast relaxation maps for each rat. Mean T_1 and T_2 values were used for further analyses. The decreasing rates of T_1 relaxation time (ΔT_1%) and T_2 relaxation time (ΔT_2%) were calculated as follows:

$$\Delta T_1\% = (T_{1pre} - T_{1post})/T_{1pre} \times 100\% \quad (2)$$

$$\Delta T_2\% = (T_{2pre} - T_{2post})/T_{2pre} \times 100\% \quad (3)$$

where T_{1pre} (or T_{2pre}) and T_{1post} (or T_{2post}) are relaxation times of pre- and post-the ultrafine SPIO@PEG injection *via* the tail vein of rat.[32]

Based on the calculated relaxation time of T_1 and T_2, we adapted the T_1 mapping and T_2 mapping sequences for the T_1–T_2 dual-mode image fusion (Fig. S3, see ESI†). Firstly, we associated the T_1 mapping and T_2 mapping images with image registration. Secondly, the pixels of ROIs in these two sequences were divided and colored *via* a "logic gate" (Fig. 7B). Thirdly, the number of positive pixels and all the pixels in ROIs were measured to calculate the PPR (PPR = the number of positive pixels/all the pixels in ROI). It is worth noting that the threshold value of the logic gate was defined as subtracting the mean reduction value of T_1 and T_2 values from the corresponding pre-contrast-enhanced T_1 and T_2 values. All the image fusion analyses were performed by using MATLAB.

2.7 Statistical analysis

All the quantitative data are shown as mean ± standard deviation. All the statistical analyses were performed by using SPSS commercial software (SPSS version 26.0, SPSS Inc., Chicago, IL). The Shapiro–Wilk test was used to analyse the distribution type, in which the parameters resulted in an approximately normal distribution. Spearman's ranked correlation test was used to investigate the correlation between the ΔCNR (ΔCNR-T_1 and ΔCNR-T_2), relaxation time parameters (T_1 values, T_2 values, ΔT_1%, and ΔT_2%), PPR, and pathological liver fibrosis stages. Unpaired Student's *t*-test or one-way analysis of variance (ANOVA) was used to compare the mean variance between

different fibrosis groups. The intraclass correlation coefficient (ICC) was used to test the consistency of signal intensity and relaxation time measurements of the two observers; ICC values less than 0.5, between 0.5 and 0.75, between 0.75 and 0.90, and greater than 0.90 represent poor, moderate, good, and excellent repeatability, respectively.[33] All tests were two-tailed, with P values less than 0.05 being considered statistically significant.

2.8 Histopathological analysis

After the MRI examination, animals were sacrificed by cervical dislocation under deep anesthesia with isoflurane, and the livers were removed and immediately fixed in 10% formalin. All the liver samples were stained with hematoxylin–eosin (HE) stain, Masson's trichrome stain, and Prussian blue stain. Pathologic analysis was regarded as the reference standard for staging rat liver fibrosis according to the METAVIR classification score system,[34] in which S0 = no fibrosis, S1 = portal fibrosis without septa, S2 = portal fibrosis and a few septa, S3 = numerous septa without cirrhosis, and S4 = cirrhosis. A pathologist with five years of experience in the diagnosis of liver pathology evaluated the stage of liver fibrosis (S0–S4) based on the standard classification mentioned before.

3 Results

3.1 Synthesis and characterization of ultrafine PEGylated superparamagnetic iron oxide

Ultrafine hydrophobic SPIO nanocrystals were synthesized by high-temperature thermal decomposition and were transferred to the aqueous phase by ligand exchange reaction (Fig. 1A). The SAED pattern of the SPIO@PEG nanocrystals is shown in Fig. S1 (ESI†). The measured lattice spacing was based on the rings in the diffraction pattern conforming to the known lattice spacing of Fe_3O_4 crystals from the PDF database. As shown in Fig. 1B, the SPIO nanocrystals have an ultrafine particle size (crystal size: 4.01 ± 0.16 nm in hexane and 5.21 ± 0.08 in water) in TEM and maintained good mono-dispersion before and after being coated with PEG-DA. FTIR spectroscopy was used to characterize the surface coating of PEG. As shown in Fig. 1C, the band around 570–590 cm^{-1} was attributed to the Fe–O stretching vibrations of the magnetite lattice. The presence of the peak at 1111.68 cm^{-1} was assigned to the asymmetric and symmetric stretching vibrations of ACH_2 of PEG-DA.[35] DLS was used to detect the hydrodynamic size distribution of the SPIO nanocrystals in hexane and PEGylated SPIO in the aqueous solution (Fig. 1D). In solution, SPIO nanoparticles had a narrow hydrodynamic size distribution, and the particle size slightly increased after PEGylation (the number average size increased from 3.19 ± 1.13 nm to 6.86 ± 2.99 nm). All the results confirmed the successful preparation of ultrafine SPIO@PEG nanoparticles. The iron concentration of SPIO@PEG aqueous solution was determined by AAS and used in subsequent experiments.

3.2 Relaxivity of ultrafine SPIO@PEG nanoparticles

To quantitively evaluate the T_1 and T_2 dual-modal MRI contrast effect of the ultrafine SPIO@PEG, the relaxivities (r_1 and r_2) of

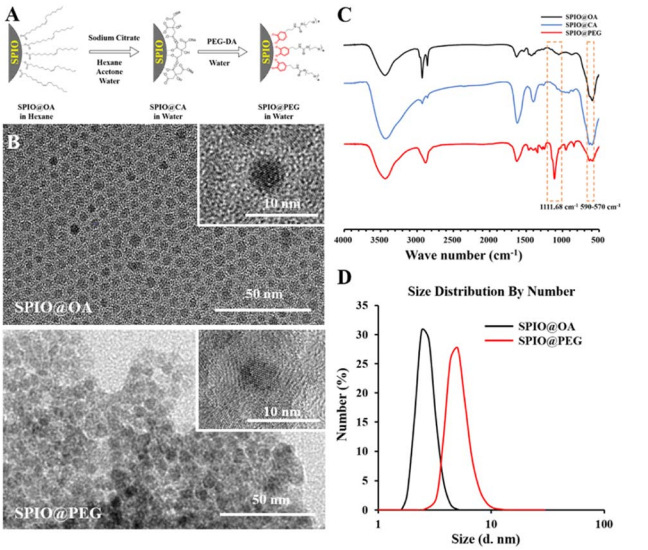

Fig. 1 PEGylated superparamagnetic iron oxide nanocrystals (SPIO@PEG). (A) A schematic representation of the preparation of SPIO@PEG. (B) Transmission electron microscopy (TEM) and HRTEM of hydrophobic oleic acid-coated SPIO (SPIO@OA) and hydrophilic PEG-coated SPIO (SPIO@PEG). (C) Fourier transform infrared (FTIR) spectra of SPIO@OA, citric acid-coated SPIO (SPIO@CA), and SPIO@PEG. (D) Dynamic light scattering (DLS) hydrodynamic size distribution of SPIO@OA (in hexane) and SPIO@PEG (in water).

aqueous samples were measured at three main different magnetic fields (0.5, 1.5, and 3.0 T). As shown in Fig. 2A and B, the ultrafine SPIO@PEG simultaneously has high r_1 and r_2. However, r_1 decreased with the increase of the magnetic field (from 0.5 to 3.0 T), while r_2 increased across the same magnetic field range, leading to the increase of the r_2/r_1 ratio. Significantly, the r_2/r_1 ratio of SPIO@PEG is 3.51 at 3.0 T, indicating that this SPIO@PEG is a T_1–T_2 dual-modal contrast agent at 3.0 T (Fig. 2C).[23] To further confirm this, FSE T_1WI and T_2WI of SPIO@PEG aqueous samples were carried out using a 3.0 T clinical MRI scanner to study the T_1–T_2 dual-modal enhancement *in vitro*. As shown in Fig. 2D, the MRI signal intensity tends to increase with the increase of concentration in SE T_1WI, while in SE T_2WI, the signal intensity tends to decrease with the increase of Fe concentration. These results confirm that ultrafine SPIO@PEG can be a proper T_1–T_2 dual-modal contrast agent with the 3.0 T MRI scanner.

3.3 Cytotoxicity assay

The toxicity of SPIO@PEG was evaluated by the cell viability assay and the cytotoxicity was estimated using Cell Counting Kit-8. SPIO@PEG nanoparticles did not show appreciable cytotoxicity at different drug loading concentrations, and there was no statistically significant difference ($P > 0.05$) compared with the blank group (without SPIO@PEG nanoparticles) as shown in Fig. 2E. All these results indicate that the ultrafine SPIO@PEG has reliable biocompatibility.

3.4 Animal model establishment and pathological results

A total of twenty-eight rats were enrolled in this study. Based on the pathological liver fibrosis stage principle,[28] five rats were

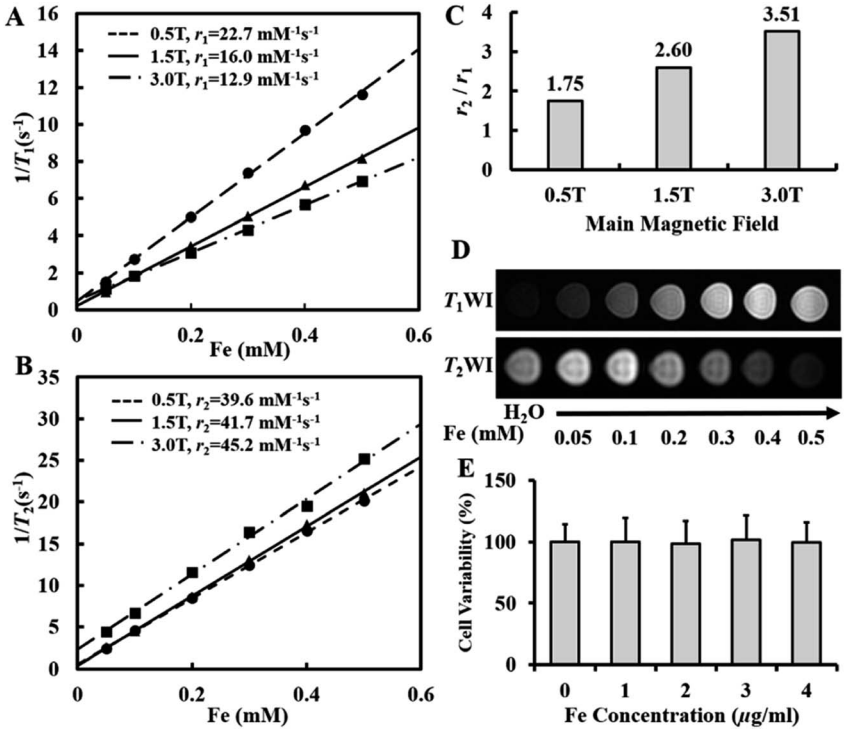

Fig. 2 MRI contrast enhancement study of PEGylated superparamagnetic iron oxide nanocrystals (SPIO@PEG) *in vitro*. (A) Longitudinal relaxation rate ($1/T_1$, s^{-1}) and (B) transverse relaxation rate ($1/T_2$, s^{-1}) as a function of Fe concentration (mM) for SPIO@PEG at 0.5, 1.5, and 3.0 T. (C) r_2/r_1 rates of SPIO@PEG at 0.5, 1.5, and 3.0 T. (D) T_1 and T_2-weighted MRI images of SPIO@PEG aqueous solution with a clinical 3.0 T MR scanner (T_1WI: spin-echo sequence, $T_R = 200$ ms, $T_E = 9$ ms, matrix = 320 × 320, field of view = 18 × 18 cm, slice thickness = 3 mm, flip angle 90°; T_2WI: spin-echo sequence, $T_R = 2500$ ms, $T_E = 100$ ms, matrix = 320 × 320, field of view = 18 × 18 cm, slice thickness = 3 mm, flip angle 90°). (E) Cell cytotoxicity assay of SPIO@PEG incubated with Hep G2 cells for 24 h. The data represent the mean ± SD.

diagnosed with stage I liver fibrosis (S1), five rats were diagnosed with stage II (S2), five rats were diagnosed with stage III (S3), and six rats were diagnosed with stage IV (S4). Seven normal rats comprised the control group. Histologic analysis with HE staining and Masson's trichrome staining demonstrated uneven distributions of liver fibrosis in the experimental rats as shown in Fig. 3.

3.5 *In vivo* contrast-enhanced MRI of liver fibrosis in the rat model

To investigate the performance of SPIO@PEG in the MRI enhancement of liver fibrosis stages, axial T_1 and T_2 weighted imaging of rat livers was obtained under a 3.0 T MRI scanner before and after the administration of the ultrafine SPIO@PEG through the tail vein. Fig. 4A shows the T_1-weighted MR imaging at different stages of liver fibrosis (S0 to S4). The post-enhanced images were brighter than the pre-contrast-enhanced images among all the groups. For the T_2-weighted MR imaging, the post-enhanced images were darker than the pre-contrast-enhanced images among the same groups (Fig. 4B). However, it failed to discriminate the different stages of liver fibrosis from visual inspection. Subsequently, we measured the SNR and CNR of liver parenchyma and quantitatively analysed the CNR changes of each rat in the two imaging modes (ΔCNR-T_1, ΔCNR-T_2). The results are shown in Fig. 4C and D. The ΔCNR-T_1 gradually increased with the progression of liver fibrosis; on the contrary, the ΔCNR-T_2 gradually decreased with the same range of liver fibrosis. Both parameters can be used to discriminate the non-fibrotic liver and stages (S ≥ 2) of liver fibrosis. However, it is challenging for these two parameters to distinguish adjacent stages of liver fibrosis.

The axial T_1 and T_2 mapping images were acquired, including pre- and post-injection of SPIO@PEG for all experimental rats. Fig. 5A and 6A have depicted that all the T_1 and T_2 mapping images display regular changes with the progression of liver fibrosis. Post-intravenous injection of SPIO@PEG, all the T_1 and T_2 values were decreased to different degrees (Fig. 5C and 6C). Moreover, both ΔT_1% and ΔT_2% decreased with the range of fibrosis stages (S0 to S4). The image fusion procession result showed that after the intravenous injection of SPIO@PEG, the PPR gradually increased with the progression of liver fibrosis. The pre-contrast enhanced PPR did not show any regular changes among the different stages of liver fibrosis (Fig. 7C).

For statistical analysis, Spearman's correlation test depicted positive correlations between the pre- and post-contrast T_1 and T_2 values and liver fibrosis stages ($r = 0.867$ and 0.940 for T_1 value, $r = 0.608$ and 0.888 for T_2 value, respectively, $P < 0.001$). PPR also showed positive correlations and liver fibrosis stages ($r = 0.979$, $P < 0.001$). Conversely, the ΔT_1% and ΔT_2% were negatively correlated to liver fibrosis stages ($r = -0.943$ and -0.784, respectively, $P < 0.001$) (Table 1).

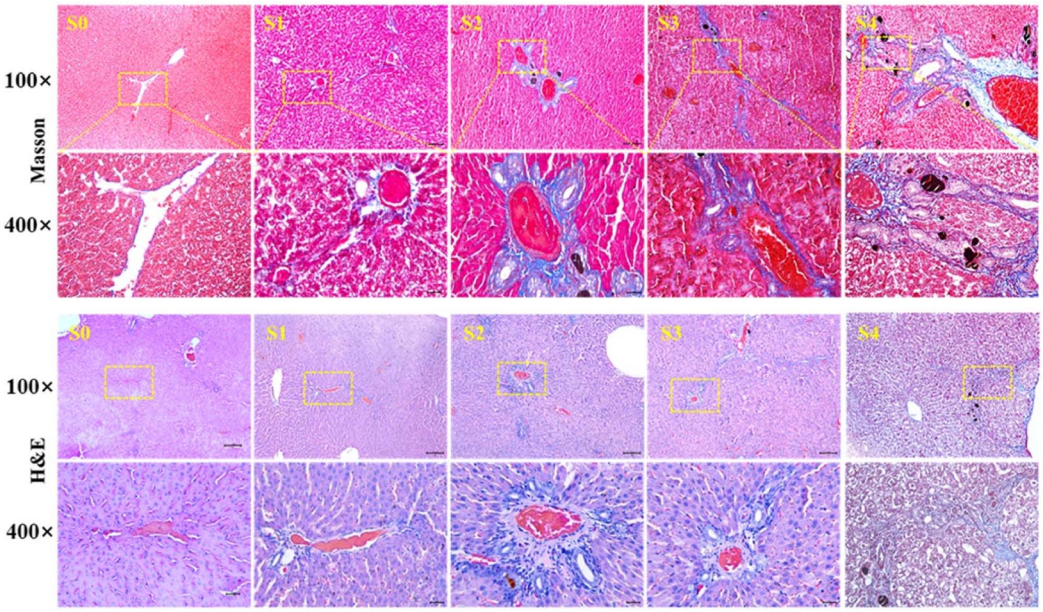

Fig. 3 Masson and H&E staining of SD rat hepatic tissues. Liver specimens were extracted for pathological examination after 0, 1, 4, 8, and 12 weeks of DDC induction, which represent the biliary fibrosis stages of S0, S1, S2, S3 and S4, respectively.

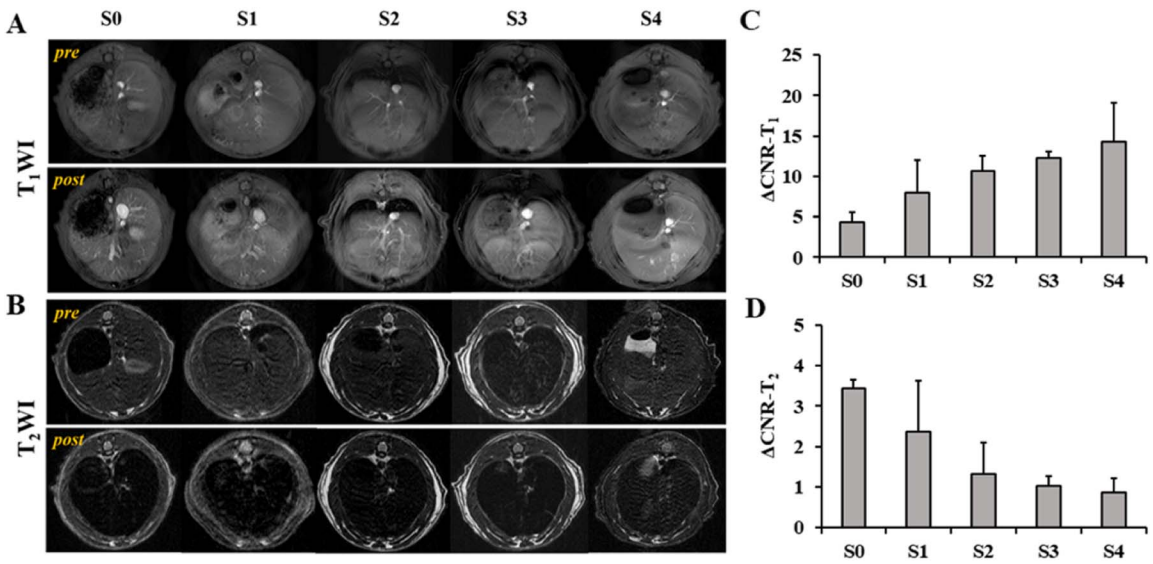

Fig. 4 T_1–T_2 dual-modal contrast-enhancement study of liver fibrosis staging in rats. (A) and (B) Conventional T_1 and T_2 weighted images (T_1WI and T_2WI) of livers at different liver fibrosis stages pre- and post-the intravenous injection of SPIO@PEG with a dose of 2.5 Fe mg kg^{-1} body-weight. Quantitative measurements of the contrast-to-noise ratio (ΔCNR) of T_1WI (C) and T_2WI (D). All the groups were compared with each other by one-way analysis of variance (ANOVA). No significant differences were found among the different groups. T_1WI: GRE sequence, $T_R = 9$ ms, $T_E = 3$ ms, FOV = 80 × 80 mm, slice thickness = 2 mm, flip angle 30°; T_2WI: FSE sequence, $T_R = 4000$ ms, $T_E = 76$ ms, FOV = 80 × 80 mm, slice thickness = 2 mm, flip angle = 90°.

Based on Spearman's correlation test, the mean differences among different liver fibrosis subgroups were determined by one-way ANOVA. For the pre-contrast T_1 and T_2 parameters, there were significant differences between the control group (S0) and any other fibrotic groups. However, there were no statistical differences between the adjacent groups ($P < 0.05$), especially among the S1, S2, and S3 subgroups (Fig. 5D and 6D). After intravenous administration of SPIO@PEG, the differences between the S2 and S3 were shown in the post-contrast T_1 values, and for S1 and S2 in post-contrast T_2 values. Nonetheless, single T_1 or T_2 parameters could not independently discriminate the stage of liver fibrosis. Moreover, the ΔT_1% and ΔT_2% were also tested by one-way ANOVA. Interestingly, the ΔT_1% differences between S0 and S1, and S2 and S3; S3 and S4 were significantly different but it was not significant between S1 and S2 stages (Fig. 5D). Notably, ΔT_2% showed a statistically

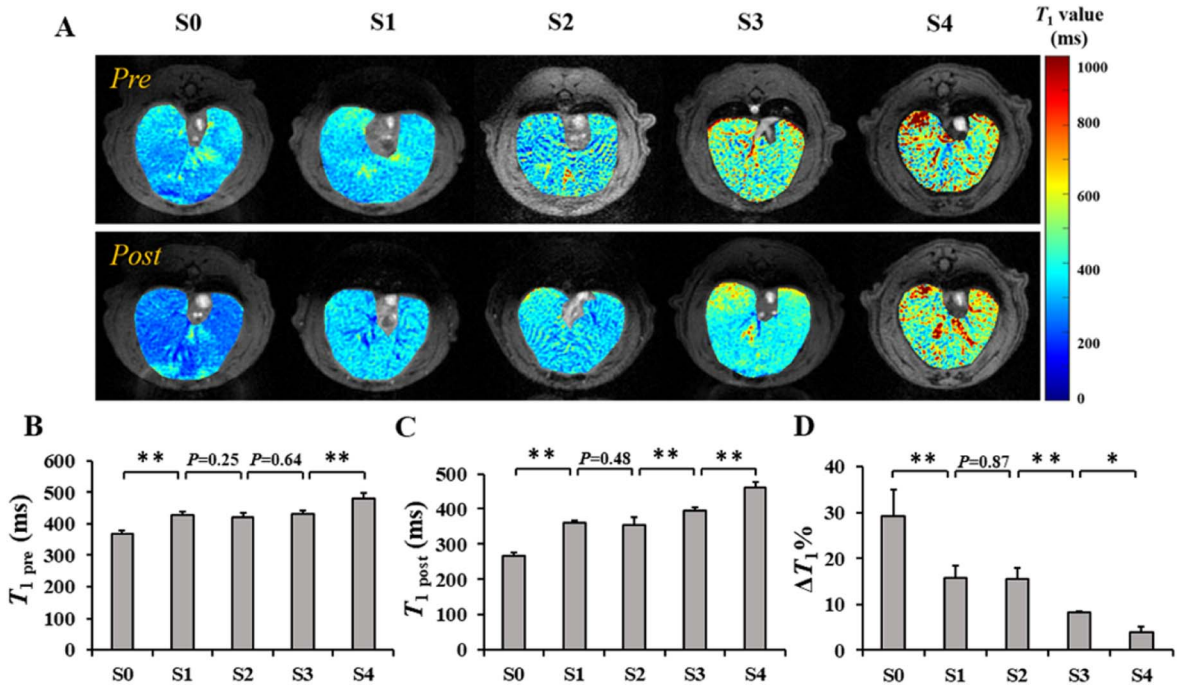

Fig. 5 Quantitative analysis of hepatic T_1 values at different stages of liver fibrosis pre- and post-administration of PEGylated superparamagnetic iron oxide (SPIO@PEG). (A) T_1 mapping images of the liver pre- and post-the intravenous injection of SPIO@PEG with a dose of 2.5 Fe mg kg^{-1} bodyweight. (B) and (C) Quantitative measurement of hepatic T_1 values at different liver fibrosis stages before (T_{1pre}) and after (T_{1post}) the administration of SPIO@PEG, and the statistical differences of all the liver fibrosis stage groups were analysed. (D) T_1 change rates (ΔT_1%) of different liver fibrosis stages and one-way ANOVA analysis results. * Refers to $P < 0.05$. ** Refers to $P < 0.01$.

significant difference between the liver fibrosis groups of S1 and S2 ($P < 0.05$) (Fig. 6D). Nevertheless, these two parameters cannot independently distinguish the different stages of liver fibrosis. For PPR analysis, there was a significant difference among all the subgroups of liver fibrosis (Fig. 7A and C). Compared with the control group (S0), other groups exhibited

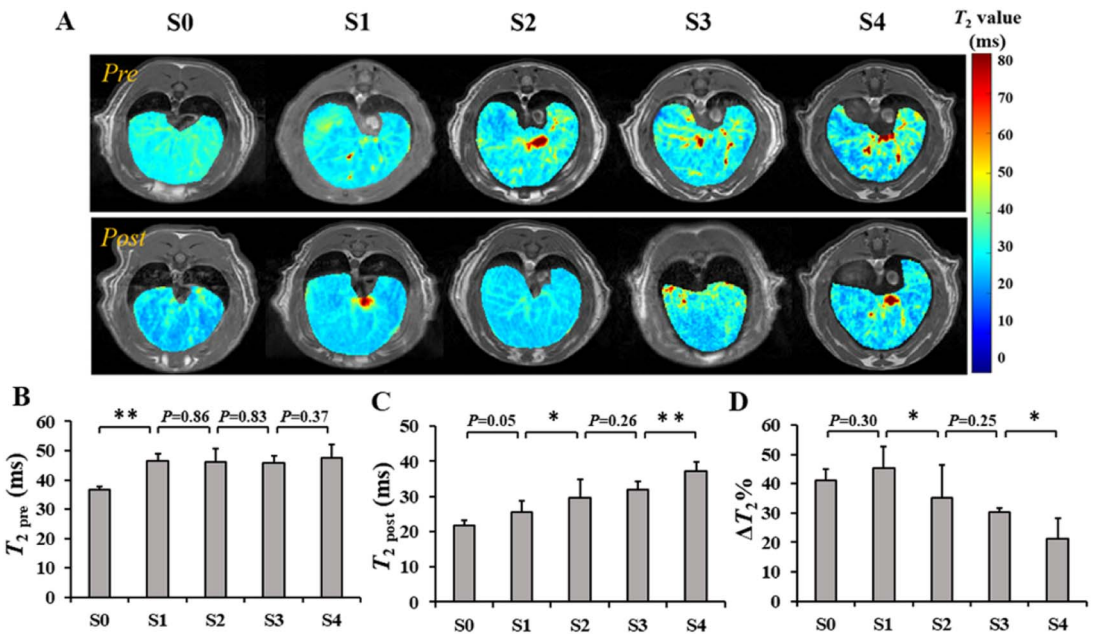

Fig. 6 Quantitative analysis of hepatic T_2 values at different liver fibrosis stages pre- and post-the administration of PEGylated superparamagnetic iron oxide (SPIO@PEG). (A) T_2 mapping of the liver pre- and post-intravenous injection of SPIO@PEG with a dose of 2.5 (Fe concentration) mg kg^{-1} bodyweight. (B) and (C) Quantitative measurement of the hepatic T_2 value at different liver fibrosis stages before (T_{2pre}) and after (T_{2post}) the administration of SPIO@PEG, and the statistical differences of all the liver fibrosis stage groups were analyzed. (D) T_2 change rates (ΔT_2%) of different liver fibrosis stages and one-way ANOVA analysis results. * Refers to $P < 0.05$. ** Refers to $P < 0.01$.

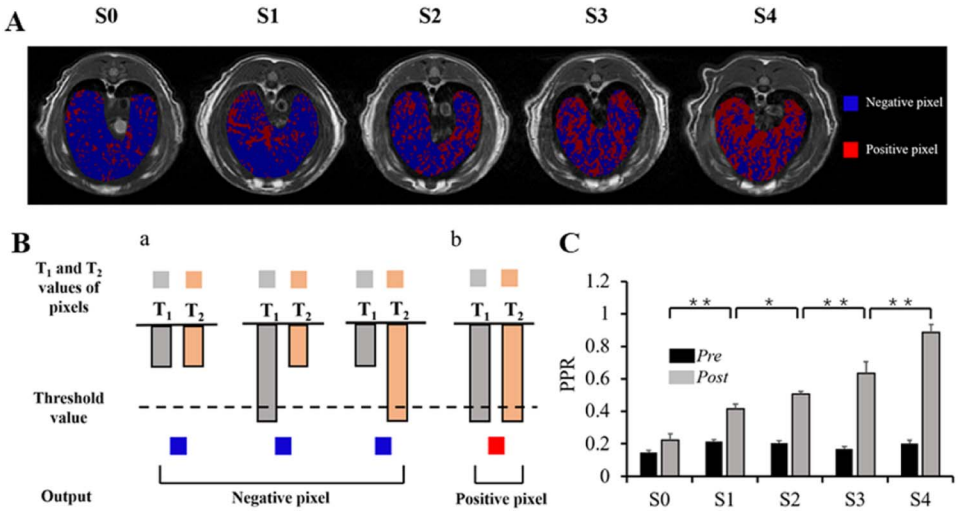

Fig. 7 Image fusion results and illustration of the logic gate process. (A) The fused images of liver fibrosis at different stages after SPIO@PEG enhanced the contrast. (B) Illustration of the logic gate process. Both T_1 and T_2 values higher than the threshold value are output as positive pixels. (a) Pixels of T_1 and T_2 mapping in either T_1 or T_2 that do not satisfy the logic gate are output as negative pixels (blue). (b) Both the pixels in T_1 and T_2 mapping that were higher than the threshold value and fulfill logic gate are output as positive pixels (red). (C) Quantitative measurements of positive pixel ratios (PPR) for different liver fibrosis stages before (pre) and after (post) the administration of SPIO@PEG. * Refers to $P < 0.05$. ** Refers to $P < 0.01$.

Table 1 The Spearman's rank correlation coefficient (r) and P value for the association between liver fibrosis stages and T_1, and T_2 values, as well as $\Delta T_1\%$ and $\Delta T_2\%$ obtained from pre- and post-SPIO@PEG contrast-enhanced magnetic resonance images[a]

Parameter	r	P
T_{1pre}	0.876	<0.001
T_{1post}	0.94	<0.001
$\Delta T_1\%$	−0.943	<0.001
T_{1pre}	0.608	<0.001
T_{2post}	0.888	<0.001
$\Delta T_2\%$	−0.784	<0.001
PPR	0.979	<0.001

[a] $\Delta T_1\% = [(T_{1pre} - T_{1post})/T_{1pre}] \times 100\%$, $\Delta T_2\% = [(T_{2pre} - T_{2post})/T_{2pre}] \times 100\%$, PPR = positive pixel ratio.

higher PPR, which increased from 0.22 ± 0.04 to 0.89 ± 0.05 with the progression of liver fibrosis.

3.6 Repeatability and reproducibility

The ICCs of the parameters including ΔCNR-T_1, ΔCNR-T_2, T_1 and T_2 pre- and post-contrast were carried out between the two observers. All the parameters showed good or excellent inter-observer agreement with repeatability and reproducibility. The ΔCNR-T_1, ΔCNR-T_2, pre- and post-contrast enhanced T_1 and T_2 relaxation times, and PPR had ICC values of 0.932, 0.943, 0.912, 0.923, 0.876, 0.897, and 0.927, respectively.

3.7 Distribution of iron nanoparticles

According to the pathological results of Prussian blue staining, the liver specimen of the control group demonstrated that the deposition of iron nanoparticles is mainly distributed in the region of the portal track and its adjacent hepatic sinus. However, iron nanoparticles are mainly deposited along the edge fibrotic septa in fibrotic groups, and few iron nanoparticles can have access to the fibrotic septa as shown in Fig. 8.

4 Discussion

The crucial element of liver fibrosis treatment efficiency relies on precise diagnosis and stage methods. T_1–T_2 dual-modal ultrafine SPIO@PEG enhanced MRI provides a non-invasive approach that combines both T_1 and T_2 contrast-enhanced information that may improve the diagnosis and staging of liver fibrosis.

This present study confirmed a strong correlation between the relaxation times of the liver fibrosis stages. Additionally, the results showed that both T_1 and T_2 relaxation times were consistently elevated with the progression of hepatic fibrosis in rats. Several human and animal studies have demonstrated that fibrosis could prolong the T_1 and T_2 relaxation times of the liver.[36–38] The prolonged T_1 and T_2 relaxation times were possibly caused by the pathophysiological alterations associated with activated liver fibrogenesis, characterized by inflammation, edema, and the excess deposition of extracellular matrix (ECM) with the degree of fibrosis.[39] In histology, biliary liver fibrosis is characterized by chronic cholangitis and mainly affects septal and interlobular bile ducts.[40] Fibrogenesis in chronic cholestatic liver diseases could be seen as a classic chronic wound-healing reaction that could directly activate fibrogenesis in liver parenchyma.[41] In the early stages, the liver parenchyma shows an intense inflammatory reaction. Moreover, the interlobular bile ducts are surrounded and infiltrated by immune/inflammatory cells causing structural damage and peribiliary stromal expansion, which could lead to a slightly

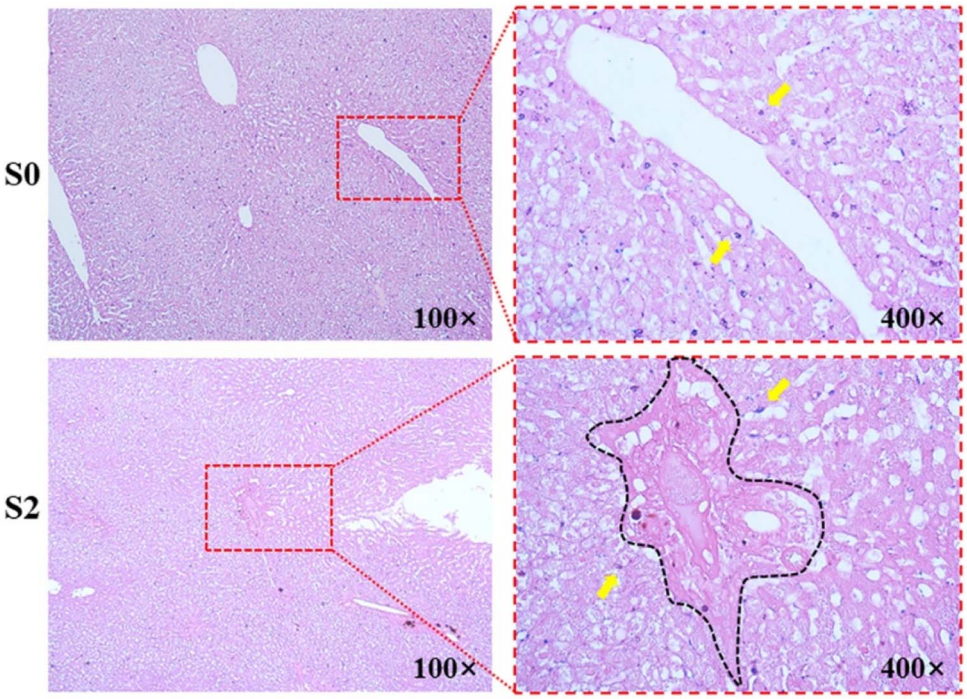

Fig. 8 Prussian blue staining of SD rat hepatic tissue after administration of PEGylated superparamagnetic iron oxide (SPIO@PEG). In the healthy group (S0), iron particles were randomly distributed in hepatic sinus (yellow arrowhead). In fibrotic groups (S2), iron particles were only distributed along the outer edge of the fibrotic septa (yellow arrowhead).

higher T_1 value in S1 than S2;[42] the portal venules are then compressed and occluded by the inflammatory reaction. In later stages, the inflammation extends to the lobule, causing the formation of fibrous septa and collagenous fiber. The pattern of collagenous fiber accumulation can be characterized by increased expression of several collagenous and non-collagenous extracellular matrix (ECM) components.[43] Collagen deposition could be the main significant influencing factor for the elevated unenhanced measurement of T_1 and T_2 values, as well as PPR. Unfortunately, our study revealed that the liver parenchyma's unenhanced T_1 and T_2 relaxation times could not accurately differentiate the liver fibrosis stages.

After intravenous administration of ultrafine SPIO@PEG nanoparticles, we found that both T_1 and T_2 values decreased by different degrees among the different liver fibrosis stages. Our study firstly demonstrated that the reduction rate of T_1 (ΔT_1%) and T_2 (ΔT_2%) both gradually decreased with the severity of the stages of biliary liver fibrosis (from S0 to S4) under T_1–T_2 dual-modal ultrafine SPIO@PEG enhanced MR images. Furthermore, the results showed significant differences between each set of adjacent hepatic fibrosis subgroups, providing potential biomarkers in precisely staging biliary liver fibrosis. However, these two parameters cannot independently distinguish the different fibrosis stages. Based on the study results of T_1 and T_2 values, we creatively fused the T_1 and T_2 mapping images and quantitively measured the PPR of each rat. Compared with the control group (S0), other groups exhibited higher PPR. Moreover, significant differences were observed among the different groups. These results collectively demonstrated the highly effective T_1–T_2 dual-mode SPIO@PEG diagnosis and staging ability for liver fibrosis.

According to the Prussian blue staining of the liver specimen after the administration of SPIO@PEG nanoparticles, we found that the iron particles were mainly deposited along the edges of fibrotic septa in fibrotic rats. The deposition of collagen fibers takes up space in the perisinusoidal space (space of Disse), leading to a variety of iron nanoparticle distributions among different fibrotic objects. The alteration of iron nanoparticle distribution leads to changes in both MR signal intensity and relaxation times among different fibrosis stages.[44] In contrast, the deposition of iron particles in the healthy liver (S0) was randomly distributed in the hepatic sinus where HSCs most commonly reside, after the administration of SPIO@PEG, on which the collagen deposition could not have an influence.

In this study, SPIO@PEG-enhanced T_1-weighted MR imaging showed a higher ΔCNR across the range of fibrosis stages S0 to S4, while the ΔCNR of T_2 became lower across the same range of fibrosis stages at 3.0 T. Tanimoto A.[45] reported that patients with chronic liver cirrhosis showed less signal intensity loss for background liver because of the poor phagocytic activity due to Kupffer cell dysfunction and therefore, the cirrhotic liver is superior as compared with the non-cirrhotic liver. We believe that the normal phagocytic function of Kupffer cells in the non-fibrotic liver can be attributed to the more significant signal intensity loss of liver parenchyma, and the incomplete phagocytic function of Kupffer cells in the fibrotic liver can be attributed to the improvement in the SNR of post-contrast T_1 weighted MR images, resulting in higher ΔCNR-T_1. On the contrary, based on

the blank hole effect of SPIO, the poor phagocytic activity of Kupffer cells in the fibrotic liver could result in a lower ΔCNR-T_2 than non-fibrotic liver on T_2-weighted MR images.

There are some advantages to our study. Firstly, the T_1–T_2 dual-modal magnetic resonance imaging combined with image fusion could avoid the false-positive signals caused by a single imaging mode and supply complementary and more accurate information for the diagnosis and staging of diseases. Secondly, in order to remove the influence of liver steatosis and ensure timely resolution, we selected the LAVA sequence to access the T_1 and T_2 values. VFA T_1 mapping has been widely studied as a potential clinical application in detecting and diagnosing liver fibrosis.[46] VFA T_1 mapping was first introduced by Fram *et al.*, which is based on a series of T_1-weighted spoiled gradient echo sequences with different flip angles.[47] At least two flip angles are required to calculate the T_1 relaxation time. However, the method of two flip angles could potentially decrease the accuracy and increase the estimation error of the T_1 value.[48] In this study, we used five flip angles to calculate the T_1 relaxation time, which could minimize the estimation error and increase the reliability of T_1 values. According to the study by Li *et al.*[36] VFA T_1 mapping is a non-invasive, reliable, and accurate imaging method for assessing experimental liver fibrosis in rodents. Compared with ultrasound elastography, it provides similar good repeatability and reproducibility, similarly high accuracy for staging fibrosis, and significantly better accuracy for detecting fibrosis regression. Thirdly, we used a 3.0 T scanner instead of a 1.5 T MR scanner for this study. The T_1 and T_2 values obtained with a 3.0 T scanner can be more accurate than with a 1.5 T scanner, which results in more reliable and accurate T_1 and T_2 values measurements in fibrotic or healthy livers. Finally, the ultrafine SPIO@PEG is a suitable T_1–T_2 dual-mode MRI contrast agent, even if there is a time lag in T_1–T_2 dual-mode imaging scanning, due to its long circulation time *in vivo* as found in our previous study.[26]

The combination of T_1 and T_2 mapping can integrate the high tissue resolution and high time resolution of T_1 mode contrast imaging and the high feasibility of soft tissue detection of T_2 mode contrast imaging.

5 Conclusions

In conclusion, we have successfully synthesized T_1–T_2 dual-modal ultrafine SPIO@PEG nanoparticles and applied them in the diagnosis and discrimination of the different stages of DDC-induced biliary liver fibrosis in the rat model. For the first time, we have demonstrated that the PPR calculated by the image fusion of T_1 and T_2 mapping could be used to discriminate different stages of biliary liver fibrosis. Furthermore, the PPR might be a noninvasive biomarker to distinguish the different stages of biliary liver fibrosis, which could be a promising non-invasive method to monitor the liver fibrosis progression and therapeutic response to the antifibrotic treatment.

Author contributions

Conceptualization, methodology, investigation, data curation, writing original draft, FLL; methodology, data curation, investigation, LD; methodology, validation, WC, HJ, YP, CWY and JW; methodology, resources, validation, TWC; resources, project administration, XMZ; supervision, writing review and editing, funding acquisition, project administration, CQW; all authors have read and agreed to the published version of the manuscript.

Conflicts of interest

There are no conflicts to declare.

Acknowledgements

The work was supported by National Natural Science Foundation of China (81601490), Natural Science Foundation of Sichuan Province (2022NSFSC0636), Science and Technology Project of Municipal School Strategic Cooperation, Nanchong (20SXQT0306), Pre-research Project of North Sichuan Medical College (CBY19-YZ05), Open Research Program of Antibiotic Research and Reevaluation Key Laboratory of Sichuan Province (ARRLKF20-03).

References

1 R. Bataller and D. A. Brenner, *J. Clin. Invest.*, 2005, **115**, 209–218.
2 M. Pinzani, M. Rosselli and M. Zuckermann, *Best Pract. Res., Clin. Gastroenterol.*, 2011, **25**, 281–290.
3 A. Ortiz-Perez, B. Donnelly, H. Temple, G. Tiao, R. Bansal and S. K. Mohanty, *Front. Immunol.*, 2020, **11**, 329.
4 S. Sakiani, D. E. Kleiner, T. Heller and C. Koh, *Clin. Liver Dis.*, 2019, **23**, 263–277.
5 C. Corpechot, F. Carrat, R. Poupon and R. E. Poupon, *Gastroenterology*, 2002, **122**, 652–658.
6 L. Castera, *Expert Rev. Gastroenterol. Hepatol.*, 2008, **2**, 541–552.
7 G. Germani, P. Hytiroglou, A. Fotiadu, A. K. Burroughs and A. P. Dhillon, *Semin. Liver Dis.*, 2011, **31**, 82–90.
8 P. C. Tien, M. Duarte, A. Roque and J. Price, *Dig. Dis. Sci.*, 2020, **65**, 928–930.
9 S. Sharma, K. Khalili and G. C. Nguyen, *World J. Gastroenterol.*, 2014, **20**, 16820–16830.
10 U. Agbim and S. K. Asrani, *Expert Rev. Gastroenterol. Hepatol.*, 2019, **13**, 361–374.
11 S. A. Harrison, V. Ratziu, J. Boursier, S. Francque, P. Bedossa, Z. Majd, G. Cordonnier, F. B. Sudrik, R. Darteil, R. Liebe, J. Magnanensi, Y. Hajji, J. Brozek, A. Roudot, B. Staels, D. W. Hum, S. J. Megnien, S. Hosmane, N. Dam, P. Chaumat, R. Hanf, Q. M. Anstee and A. J. Sanyal, *Lancet Gastroenterol. Hepatol.*, 2020, **5**, 970–985.
12 N. Perakakis, K. Stefanakis and C. S. Mantzoros, *Metabolism*, 2020, **111S**, 154320.
13 R. Masuzaki, T. Kanda, R. Sasaki, N. Matsumoto, M. Ogawa, S. Matsuoka, S. J. Karp and M. Moriyama, *Int. J. Mol. Sci.*, 2020, **21**, 4906.
14 Y. Yang, J. Wu, S. Huang, Y. Fang, P. Lin and Y. Que, *IEEE J. Biomed. Health Inform.*, 2019, **23**, 1647–1660.

15 R. Zhao, G. Hamilton, J. H. Brittain, S. B. Reeder and D. Hernando, *Magn. Reson. Med.*, 2021, **85**, 734–747.
16 R. Zhao, D. Hernando, D. T. Harris, L. A. Hinshaw, K. Li, L. Ananthakrishnan, M. R. Bashir, X. Duan, M. A. Ghasabeh, I. R. Kamel, C. Lowry, M. Mahesh, D. Marin, J. Miller, P. J. Pickhardt, J. Shaffer, T. Yokoo, J. H. Brittain and S. B. Reeder, *Med. Phys.*, 2021, **48**, 4375–4386.
17 J. Wang, Y. Jia, Q. Wang, Z. Liang, G. Han, Z. Wang, J. Lee, M. Zhao, F. Li, R. Bai and D. Ling, *Adv. Mater.*, 2021, **33**, e2004917.
18 M. T. Long and E. J. Benjamin, *Circ.: Cardiovasc. Imaging*, 2018, **11**, e007553.
19 S. Pan, X. Q. Wang and Q. Y. Guo, *World J. Gastroenterol.*, 2018, **24**, 2024–2035.
20 Y. D. Xiao, R. Paudel, J. Liu, C. Ma, Z. S. Zhang and S. K. Zhou, *Int. J. Mol. Med.*, 2016, **38**, 1319–1326.
21 W. Xie, Z. Guo, F. Gao, Q. Gao, D. Wang, B. S. Liaw, Q. Cai, X. Sun, X. Wang and L. Zhao, *Theranostics*, 2018, **8**, 3284–3307.
22 M. Doig, C. P. Warrens and P. J. Camp, *Langmuir*, 2014, **30**, 186–195.
23 Z. Zhou, R. Bai, J. Munasinghe, Z. Shen, L. Nie and X. Chen, *ACS Nano*, 2017, **11**, 5227–5232.
24 Z. Zhou, Z. Zhao, H. Zhang, Z. Wang, X. Chen, R. Wang, Z. Chen and J. Gao, *ACS Nano*, 2014, **8**, 7976–7985.
25 Z. Zhou, C. Wu, H. Liu, X. Zhu, Z. Zhao, L. Wang, Y. Xu, H. Ai and J. Gao, *ACS Nano*, 2015, **9**, 3012–3022.
26 L. H. Deng, H. Jiang, F. L. Lu, H. W. Wang, Y. Pu, C. Q. Wu, H. J. Tang, Y. Xu, T. W. Chen, J. Zhu, C. Y. Shen and X. M. Zhang, *Int. J. Nanomed.*, 2021, **16**, 201–211.
27 S. Sun, H. Zeng, D. B. Robinson, S. Raoux, P. M. Rice, S. X. Wang and G. Li, *J. Am. Chem. Soc.*, 2004, **126**, 273–279.
28 P. Fickert, U. Stoger, A. Fuchsbichler, T. Moustafa, H. U. Marschall, A. H. Weiglein, O. Tsybrovskyy, H. Jaeschke, K. Zatloukal, H. Denk and M. Trauner, *Am. J. Pathol.*, 2007, **171**, 525–536.
29 S. C. Deoni, B. K. Rutt and T. M. Peters, *Magn. Reson. Med.*, 2003, **49**, 515–526.
30 F. Siedek, A. M. Muehe, A. J. Theruvath, R. Avedian, A. Pribnow, S. L. Spunt, T. Liang, C. Farrell and H. E. Daldrup-Link, *Eur. Radiol.*, 2020, **30**, 1790–1803.
31 M. Beaumont, I. Odame, P. S. Babyn, L. Vidarsson, M. Kirby-Allen and H. L. Cheng, *J. Magn. Reson. Imaging*, 2009, **30**, 313–320.
32 R. F. Sheng, H. Q. Wang, L. Yang, K. P. Jin, Y. H. Xie, C. X. Fu and M. S. Zeng, *Dig. Liver Dis.*, 2017, **49**, 789–795.
33 T. K. Koo and M. Y. Li, *J. Chiropr. Med.*, 2016, **15**, 155–163.
34 T. Poynard, P. Bedossa and P. Opolon, *Lancet*, 1997, **349**, 825–832.
35 G. Prabha and V. Raj, *Biomed. Pharmacother.*, 2016, **80**, 173–182.
36 J. Li, H. Liu, C. Zhang, S. Yang, Y. Wang, W. Chen, X. Li and D. Wang, *Eur. Radiol.*, 2020, **30**, 337–345.
37 J. A. Luetkens, S. Klein, F. Traber, F. C. Schmeel, A. M. Sprinkart, D. L. R. Kuetting, W. Block, F. E. Uschner, R. Schierwagen, K. Hittatiya, G. Kristiansen, J. Gieseke, H. H. Schild, J. Trebicka and G. M. Kukuk, *Radiology*, 2018, **288**, 748–754.
38 A. M. Chow, D. S. Gao, S. J. Fan, Z. Qiao, F. Y. Lee, J. Yang, K. Man and E. X. Wu, *J. Magn. Reson. Imaging*, 2012, **36**, 152–158.
39 D. H. Hoffman, A. Ayoola, D. Nickel, F. Han, H. Chandarana and K. P. Shanbhogue, *Abdom. Radiol.*, 2020, **45**, 692–700.
40 M. Pinzani and T. V. Luong, *Biochim. Biophys. Acta, Mol. Basis Dis.*, 2018, **1864**, 1279–1283.
41 N. S. Ghonem, D. N. Assis and J. L. Boyer, *Hepatology*, 2015, **62**, 635–643.
42 A. F. Gulamhusein and G. M. Hirschfield, *Nat. Rev. Gastroenterol. Hepatol.*, 2020, **17**, 93–110.
43 A. Lleo, S. Marzorati, J. M. Anaya and M. E. Gershwin, *Hepatol. Int.*, 2017, **11**, 485–499.
44 J. Y. He, W. H. Ge and Y. Chen, *World J. Gastroenterol.*, 2007, **13**, 2061–2065.
45 A. Tanimoto, Y. Yuasa, H. Shinmoto, M. Jinzaki, Y. Imai, S. Okuda and S. Kuribayashi, *Radiology*, 2002, **222**, 661–666.
46 Y. Choi, J. Huh, D. C. Woo and K. W. Kim, *Br. J. Radiol.*, 2016, **89**, 20150666.
47 E. K. Fram, R. J. Herfkens, G. A. Johnson, G. H. Glover, J. P. Karis, A. Shimakawa, T. G. Perkins and N. J. Pelc, *Magn. Reson. Imaging*, 1987, **5**, 201–208.
48 H. Kuribayashi, M. Sekino, T. Minowa, Y. Maitani, H. Ohsaki, S. Tsushima, S. Hirai, M. Ueda and Y. Katayama, *J. Magn. Reson. Imaging*, 2013, **38**, 1245–1250.